MODIS-based Mosaic of Antarctica (MOA) data sets: Continent-wide surface morphology and snow grain size

T.A. Scambos [a],*, T.M. Haran [a], M.A. Fahnestock [b], T.H. Painter [a], J. Bohlander [a]

[a] *National Snow and Ice Data Center, Cooperative Institute for Research in Environmental Sciences, 1540 30th Street, University of Colorado, Boulder Boulder, CO 80309-0449, United States*
[b] *Institute for the Study of Earth, Oceans, and Space 461 Morse Hall, University of New Hampshire, Durham, NH 03824, United States*

Abstract

We present digital image mosaics of surface morphology and optical snow grain size for the Antarctic continent and surrounding islands, assembled from 260 Moderate-resolution Imaging Spectroradiometer (MODIS) images. The products are derived from MODIS band 1 (red light: ∼647 nm) and band 2 (infrared: ∼857 nm) orbit swath data acquired during the 2003–2004 austral summer. Multiple images of all areas are combined in a data cumulation scheme to improve spatial resolution and increase radiometric content of the mosaics. The component images were de-striped, geo-registered, and re-sampled to the projection grid using the MODIS Swath-to-Grid Toolbox (MS2GT) software. A 125 m ground-equivalent polar stereographic projection was used, identical to previous radar image mosaics and similar to several other continent-wide data sets. Geo-location accuracy of the final mosaics is better than 125 m. Swath acquisition times were limited to the range 05:00–13:30 UT to provide broad but uniform mosaic illumination. Regions of cloud cover, blowing snow, and intense forward scattering were masked prior to compositing. The MOA snow grain size data set image provides the first continent-wide semi-quantitative map of mean summer snow, firn, and blue ice grain size. Optical grain size (radius) was determined using a normalized difference index derived from MODIS band 1 and band 2 rad values. Atmospheric correction, adjustments for directional reflectance variation and snow grain size estimation were accomplished by a look-up table, generated by a combination of published models of snow spectral reflectance and atmosphere radiative transfer. Validation of the snow grain size image is provided by in situ spectra of snow-covered sea ice made in October, 2003. We use the new data sets to determine major ice shelf areas, and shelf edge, coastline, and ice grounding line vector files, and determine areas of selected blue ice regions. These data sets are available for download at http://nsidc.org/data/moa/.
© 2007 Published by Elsevier Inc.

Keywords: Antarctica; MOA; Surface morphology; Snow grain size; MODIS; Data cumulation

1. Introduction

The ability of visible and near-infrared (VIS-NIR) satellite sensors, notably the Landsat series and the Advanced Very High Resolution Radiometer (AVHRR), to reveal previously un-known features of the Antarctic continent and its coastline was broadly recognized in the 1980s by glaciologists and carto-graphers (e.g., Bindschadler et al., 1988; Crabtree & Doake, 1980; Dowdeswell & McIntyre, 1987; Merson, 1989; Sim-monds, 1986; Stephenson and Bindschadler, 1990; Swithin-bank, 1988). Later, a host of studies showed how careful processing of image radiometry could provide unprecedented information about the ice sheet surface, revealing details of ice flow, sub-ice bedrock structure, and wind-related features in the interior of the ice sheet simply by detailed portrayal of the subtle surface morphology — even at the ∼1 km spatial resolution scale of AVHRR (Bindschadler & Vornberger, 1990; Fahnestock et al., 2000a; Orheim & Lucchitta, 1988; Scambos & Bindschadler, 1991; Seko et al., 1993). The U. S. Geological Survey created continent-wide mosaics using AVHRR (Ferrigno et al., 1996; USGS, 1991); USGS and other groups then created regional ice feature image maps using Landsat (e.g., Ferrigno et al., 1994; Swithinbank et al., 1988). Recognizing that a red-

* Corresponding author. Tel.: +1 303 492 1113.
 E-mail address: teds@icehouse.colorado.edu (T.A. Scambos).

infrared band combination can provide grain size information, Winther et al. (2001) used the VIS-NIR data from the USGS/Ferrigno AVHRR mosaics to generate an approximate estimate of total blue ice area for the continent. This followed earlier experiments at mapping snow grain size and blue ice extent from space (e.g., Bourdelles & Fily, 1993; Orheim & Lucchitta, 1990). More recently, mosaics using synthetic aperture radar have been compiled (e.g., Fahnestock et al., 1993; Jezek, 1999), providing a unique view of the backscatter of the surface layer (up to ~20 m depth) over the continent. This active sensor type, operating at wavelengths nearly unaffected by clouds, permits a

great deal of control over the assembly of the continent-wide image. However, surface morphology is muted and overprinted by a strong volume scattering component coming from deeper structures such as melt layers, coarse hoar crystals, or annual snow layering.

Compiling a uniform continent-wide satellite image mosaic using VIS-NIR data presents a number of challenges (see Bohlander et al., 2004). The Antarctic continent combines low-contrast ice-dynamics-related features in the interior with high-contrast mountain and dry valley areas near the coast. Being a polar target, there are several considerations regarding image
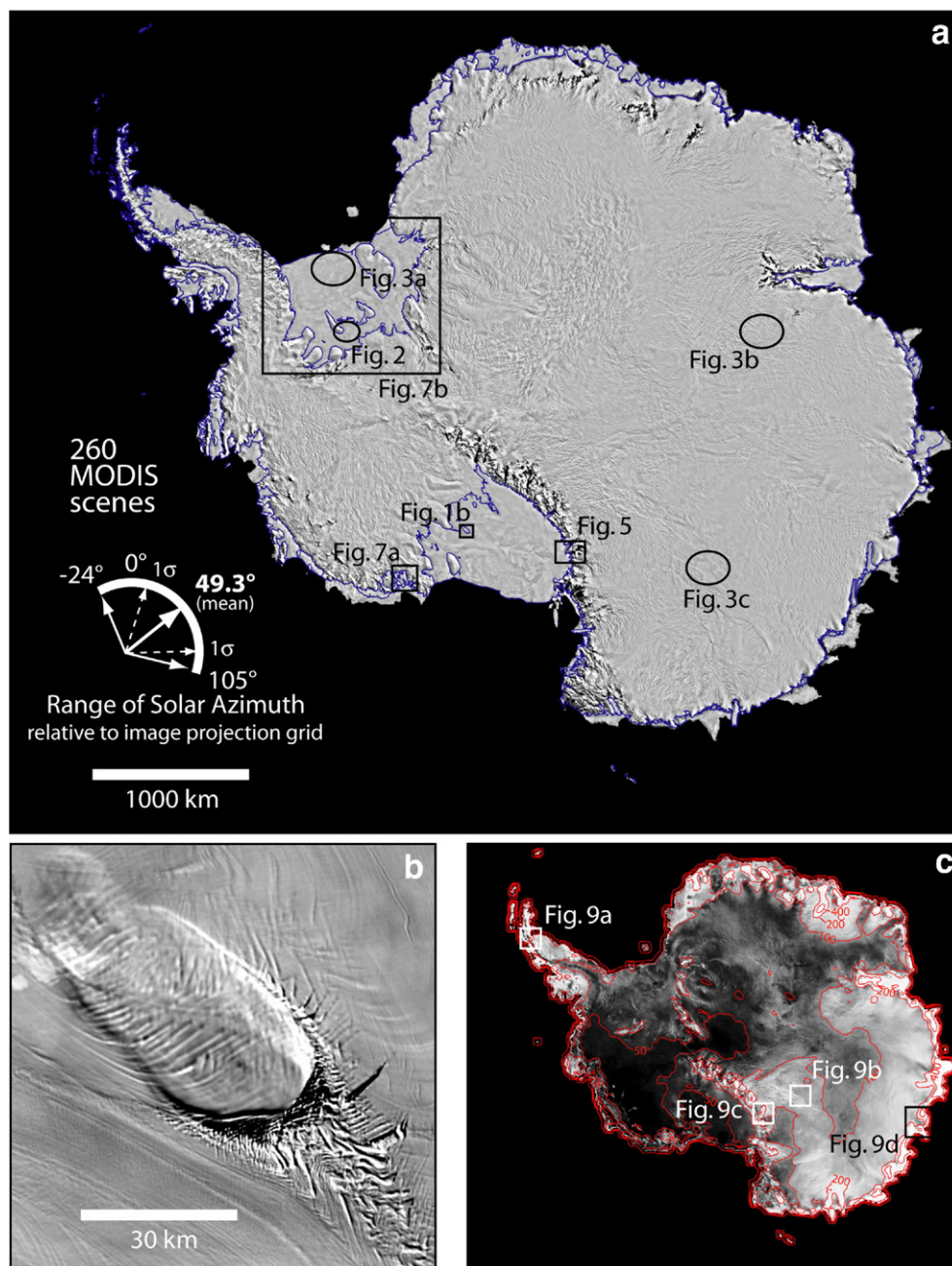

Fig. 1. (a) MOA surface morphology image with MOA-derived coastline and grounding line in blue; (b) Sub-scene showing full resolution detail from the surface morphology mosaic over Steershead Ice Rise; (c) MOA surface grain size image. In (a), sub-scenes locations for (Figs. 2, 3, 5, and 7) are indicated, as well as a graphical representation of the mean solar azimuth. A single image at a solar azimuth angle of −53.7° was used for Peter I Island (not shown in inset diagram).

acquisition, solar elevation and azimuth, visible-light scattering off the snow surfaces, and the latitudinal limits and off-nadir degradations of the sensor. Clouds, cloud shadows, and blowing snow must be identified and removed, and the images combined seamlessly with uniform histograms.

Here we present Antarctic continent-wide mosaic image data sets of surface morphology and mean snow grain size using 260 cloud- and noise-cleared Moderate-resolution Imaging Spectroradiometer (MODIS) scenes, and explore some of their applications (Fig. 1). MODIS offers higher spatial and radiometric resolution than AVHRR, and there are two active MODIS sensors (on NASA's Terra and Aqua satellites) during the period of compilation. We combine several techniques previously used, and some new methods, to improve the accuracy, detail, and seamlessness of the mosaic image data sets.

2. Image selection, processing, and compilation of the mosaic

The 260 MODIS orbital swath images were acquired over the austral summer season between November 20 2003 and February 29 2004. Image selection was restricted to a UT time range of 05:30 to 13:30, thus constraining illumination direction to a relatively narrow range, from the top, upper right, and right side in the image projection (some exceptions to this UT range were made to gather Antarctic island data swaths for the composite). The restricted illumination range results in a more uniform representation of mountains, and a nearly seamless composite image of subtle ice topography across the continent. However, since the surface is illuminated over a range of solar azimuths, linear features of all orientations are more clearly visible.

A restricted UT range requires acquisition over the full range of *local* times over the continent, and thus results in wide variations of solar elevation. Over the northern West Antarctic coastline, e.g. near 135° W longitude, the selected UT range occurs around local midnight. This means that visible-near-infrared (VIS-NIR) images must be acquired near austral summer solstice to provide an adequate solar elevation (3–20°). At the opposite side of Antarctica, in Enderby Land, a near-solstice image has a solar elevation of up to 45°. High solar elevation reduces the amount of topographic detail in a VIS-NIR image. To moderate this effect, and to create a more uniform mosaic, we selected images with an approximate gradation in acquisition dates across the continent: near solstice for areas near 135° W longitude, mid January images for the central Antarctic, and late summer images (late January–February) for the Enderby Land area. In our final composite images, mean solar elevation is 23.6°±7.7° (1σ), with a minimum of 3.6° and maximum of 47.2°; 99.9% of the composite pixels have mean solar elevation values between 5.1° and 41.6°.

2.1. Geo-registration and image processing

Satellite image data swaths of Band 1 (620–670 nm) and Band 2 (841–876 nm from MODIS Level 1B MOD02QKM (Terra) and MYD02QKM (Aqua) files, together with illumination and viewing angle data from Level 1A MOD03 and MYD03 files, were geo-located and re-sampled onto the projection grid using the MS2GT software available from the National Snow and Ice Data Center (http://nsidc.org/data/modis/ms2gt). Geolocation information, including surface positioning incorporating elevation data from the Global 30 Arc-Second Digital Elevation Data Set (GTOPO30) is present in the MOD03 and MYD03 files. MS2GT interpolates the 1 km resolution latitude and longitude data from the Level 1A files to 250 m resolution, and then re-samples the Level 1B data to the selected polar stereographic 125 m grid using a forward elliptical weighted average algorithm (Greene and Heckbert, 1986). Additionally, we generated all data products, 'browse' versions of the component scenes and several meta-data files at a 750 m grid resolution in the same projection.

Accuracy of the Level 1A geo-location data is estimated at 50 m (Wolfe et al., 2002), i.e., considerably better than the ground-equivalent nadir pixel size for the MODIS bands (∼250 m). Several tests of this geo-location accuracy and precision were conducted using known-location surface sites (e.g. South Pole Station, Vostok Station, Dome Concordia camp, Megadunes 2003–2004 camp, Siple Dome camp and its north–south GPS traverse trail) and areas of accurately mapped coastline (e.g., Ross Island, northern Antarctic Peninsula). Additionally, a thorough comparison with the RAMP AMM-1 (Radarsat Antarctic Mapping Project Antarctic Mapping Mission-1) image was conducted, which has an estimated continent-wide geo-location accuracy of ∼ 50 m (Jezek, 1999). In no case did we find a discrepancy of >125 m (i.e., one grid cell) in the projected location of a fixed object among the 260 scenes, or relative to well-mapped fixed coastline positions. Further, overlapping areas of separate images showed the same feature locations on the grid to within one grid cell. Thus, in areas where the mapped coast positions differ from the MOA image, we conclude that the MOA coast is more accurate, e.g., relative to the CIA World Vector coastline, or the Antarctic Digital Database (http://www.add.scar.org).

2.2. De-striping of MODIS image data

The MS2GT software includes an algorithm for removal of a number of artifacts in the two MODIS 40-detector whiskbroom scanners and the two mirror sides of each MODIS sensor (Fig. 2; Haran et al., 2002). The intra-detector variations are as large as 1%, or 50 DN (data numbers) in the 12-bit MODIS data, leading to pronounced horizontal striping, and a periodic 'stitching' sequence of bright-dark pixel pairs, in highly contrast-enhanced images. The striping pattern appears to be due to uncorrected calibration differences among the 40 detectors. A secondary variation in brightness appears between successive 40-line scans that is probably due to mirror side reflectance differences in the double-sided MODIS scan mirror. The 'stitching' artifact appears as an every-fourth-pixel brightness shift of up to 100 DN in detectors 27, 28 and 29 in the Terra MODIS sensor. These three artifacts must be addressed for the low-contrast ice sheet interior areas because they introduce brightness variations as large or larger than the shading due to the subtle surface morphology, and would also impact optical snow grain size calculations.

To correct the problem, a solar zenith angle normalization is conducted on the swath data for both bands. Then a column interpolation is performed on the detector 27, 28 and 29 data, using both the brightness-shifted pixels and the adjacent pixels on either side. With 'stitching' corrected, the scan artifact is addressed by evaluating the difference of each of the 40 detectors, and the two mirror sides, with the mean reflectance of the entire swath image. We treat the 40-detector and two-mirror-side system as 80 separate data sets for this step. A relative gain and offset for each of the 80 scan lines is determined by a linear regression of the data from the scan line to the data from the entire image, i.e., normalizes all the gains and offsets to the mean, creating a partially corrected image. This set of 80 regressions is followed by 6 more passes of 80 regressions each. In each pass, each scan line is compared to the mean of a group of scan lines including the target scan line. The group size begins at 2, then increases to 4, 8, 20, 40, and 80 for the subsequent passes. After each regression, the calculated gains and offsets are applied to each pixel in the scan line. The final result is a corrected swath image. De-striped images have residual linear variations of 3 to 5 DN. Missing lines and telemetry noise in the MODIS swath images, the latter having the appearance of 'chads', or small rectangles of non-sensor values in the projected scenes, were identified and reset to the mask value (i.e. treated as masked cloud or artifact areas).

Following de-striping, each swath image is re-sampled to one or more tiles comprising a polar stereographic projection grid. The projection uses the WGS-84 ellipsoid datum, with the 0°–180° longitude line parallel to the *y*-axis and the plane of the projection defined by the 71°S latitude line on the ellipsoid. For the 125 m projection, we used 16 tiles to reduce the computer memory requirements during assembly; the overall projection is 48,333 by 41,779 grid cells. For the 750 m projection, a single 8056 by 6964 tile was used.

2.3. Masking of clouds, cloud shadows, and other artifacts

The gridded swath images were manually masked to remove clouds, cloud shadows, fog, blowing snow, and heavy surface frost (no automated routine is available, or identifiable, to mask this group of image obscurations). To do this, the images were compared to the RAMP AMM-1 SAR (synthetic aperture radar) mosaic image (http://nsidc.org/data/ramp/; also Jezek, 1999), and to initial versions of the MOA composite, to identify cloud, fog, and blowing snow areas. Cloud and surface artifact masking was conducted using the 750 m grid images, and then the same mask was expanded and applied to the 125 m scenes. Some small cloud and fog features at <750 m scale were not masked, and in a few persistently cloudy areas some thin cloud and cloud-shadow
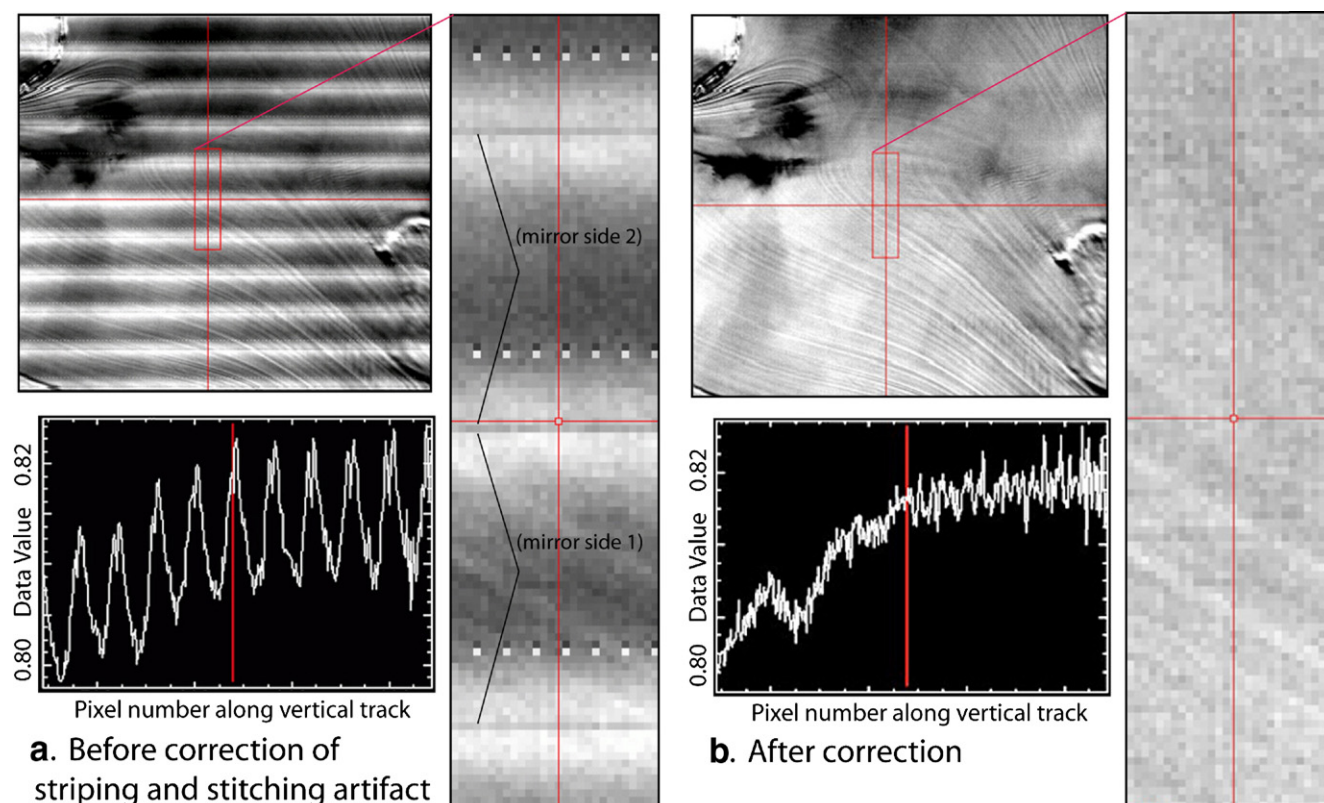

Fig. 2. Striping and 'stitching' artifact from the MODIS sensor (left) and results of the correction algorithm (right). Upper left of both image groups is a sub-scene from a MODIS Terra band 2 image of the Ronne Ice Shelf. Vertical red line is the location of a pixel value profile across the image scan lines, and the elongate red box near the center is the area of the expanded sub-scene at the right of both image groups. The plots at the lower left depict pixel value (solar-zenith-angle corrected top-of-the-atmosphere reflectance) versus pixel row number, illustrating the final results of the multi-step de-striping algorithm. Mirror-side groups are shown in the left-hand image; however, mirror-side differences are not visible at this stage of the processing. (For interpretation of the references to colour in this figure legend, the reader is referred to the web version of this article.)

contaminated images had to be used to completely cover the continent with multiple scenes (e.g. northeastern Ronne).

The mosaic composite is very nearly perfectly cloud-cleared. Some areas of thin cloud, cirrus cloud shadow and fog or low-lying small clouds are present in the northeastern Ronne Ice Shelf, which was persistently cloudy throughout the 2003–2004 austral summer. Other known sites of remaining cloud are at the grounding line near Bailey Ice Stream (Fig. 3a; 79.67°S, 33.1°W), the ice tongue of Jutulstraumen Glacier (70°S, 0°E), and Mobiloil Inlet and the adjacent Solberg Inlet (68.4°S, 66.5°W). In numerous areas, there are small patchy clouds and shadows of <~1 km size as a result of using the 750 m-resolution images for cloud evaluation and masking. We identified what we assume are blowing snow features in several
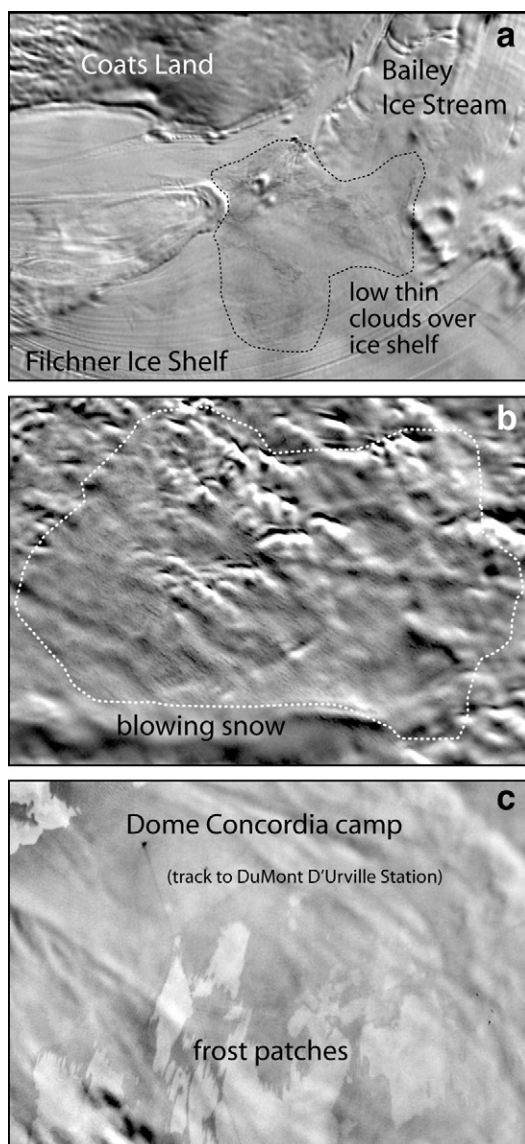

Fig. 3. Examples of remaining artifacts in the MOA surface morphology image: a.) small, thin cloud artifacts in northern Ronne Ice Shelf; b.) blowing snow and shadows from snow plumes in East Antarctica (American Highland); c.) surface hoar frost patches near Dome Concordia station. All three image areas are 112.5 by 80 km.

areas on a larger scale (up to 100s km²), particularly in East Antarctica over the upper slopes of the ice sheet. Blowing snow appears as a low-contrast mottling of the undulation surface (e.g., Fig. 3b), often with lineations in the mottling oriented near the mean katabatic wind direction (e.g., Parrish & Bromwich, 1991). Also widespread are low-contrast artifacts from hoar frost patches. These are regions where fog or emerging vapor from the snowpack have formed frost crystals on the surface (Fig. 3c). The appearance is sharp-edged patches, often with a sawtooth or flame-like outline, that in general cross-cut the undulations or other topography on the ice surface. Selecting late spring or early summer images where possible, and averaging images acquired over a wide period of time (frost patches change on a scale of days) reduces the number of hoar patches and their intensity in the final image. Fig. 3 provides examples of the known artifacts remaining in the MOA surface morphology image. We are compiling a list of clouds and other blemishes in the MOA data sets on the distribution website (see below), and seek contributions from users.

2.4. Generation of the Mosaic Data Product Images

After de-striping, geo-location, and mask generation, we created two composite images from the MODIS band 1 and band 2 data: a high-pass filtered band 1 image composite (Fig. 1a and b), detailing the surface morphology; and a mean optical snow grain size image (Fig. 1c). We additionally generated ancillary images related to final image quality (see Fig. 4): image count (number of images contributing to each grid cell in the final images); and mean pixel weight (the average 'weight' or observation quality value, applied to the pixels that contributed to each grid cell). We discuss the processing and assembly steps of these two composites separately below.

2.4.1. Surface morphology composite

The masked gridded band 1 images were high-pass filtered to reduce non-Lambertian reflection effects over snow and firn and to set the mean greyscale of the component images to a common value for more seamless compositing (we use the integer 16,000; i.e., near the mid-range of positive values for a 2-byte binary data field). Filter kernel size was 511 by 511 pixels, or about 64 by 64 km ground equivalent. Note that spatial features larger than this scale have a suppressed representation in the final grid; however, most ice-dynamic features (e.g., inter-stream ridges and ice domes), and all rock and ice shelf features, have spatial scales smaller than this size. Filtering (and all other processing) was conducted with the data as either two-byte integer or four-byte floating-point values to preserve relative radiometric variations.

Several steps were taken in the filtering algorithm to preserve contrast details of all surface types (rock, ice, dirt, and snow), and to reduce the 'overshoot' effects of spatially filtering high-contrast boundaries. First, mask values (integer value 0) were ignored by the filter algorithm. Second, we applied several within-kernel statistical tests to eliminate the effects of small (relative to the kernel size) dark nunataks within the ice fields, or patchy snow against a dark rock background. These tests
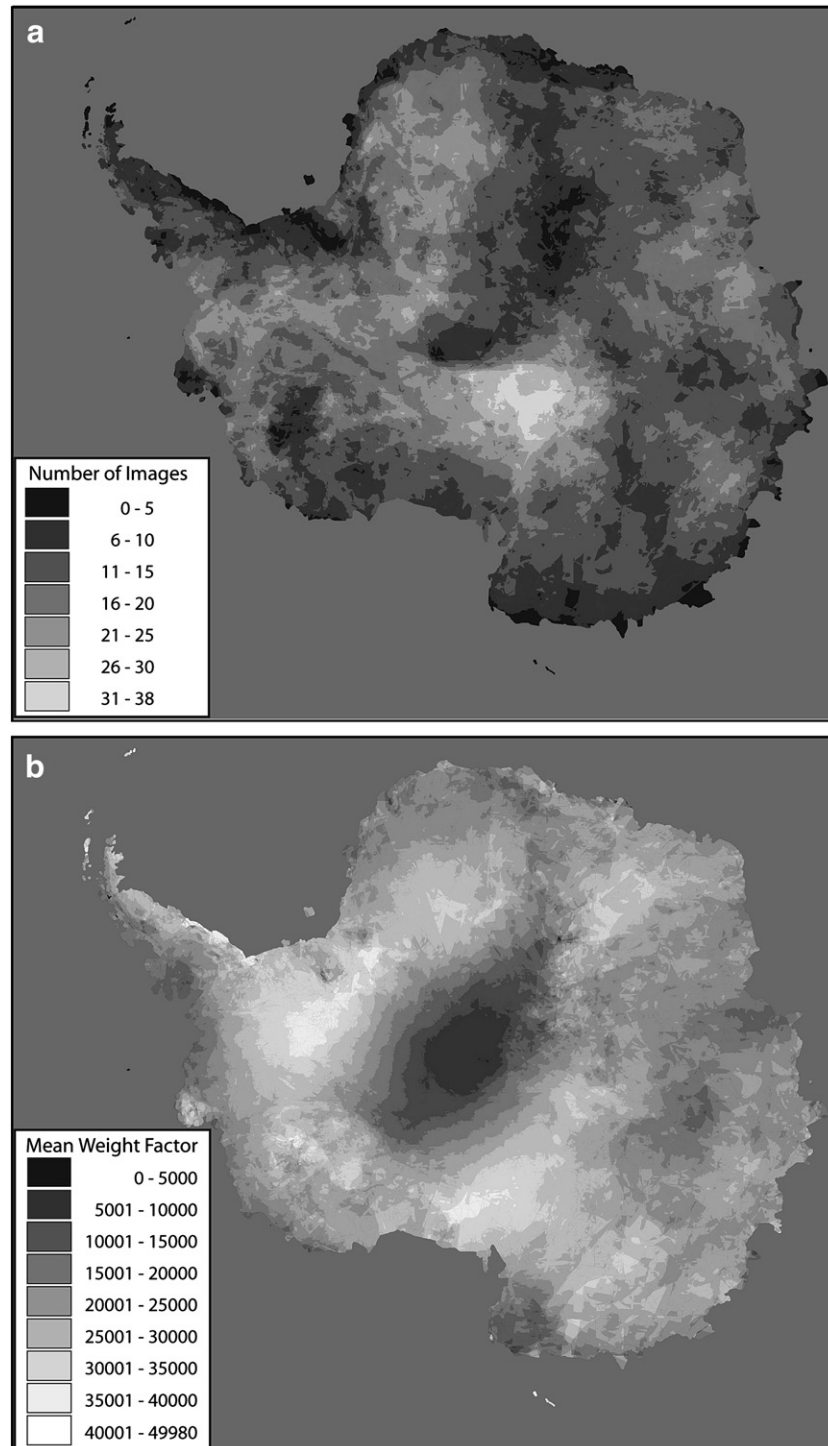
Fig. 4. (a) Image count map for the final MOA surface morphology mosaic; (b) Mean weight of contributing images for the final MOA surface morphology mosaic. Weight values have been multiplied by a scaling factor of 50,000. Image count and mean weight images for the snow grain size data set are very similar but are not shown.

consisted of elimination of outlier pixels on the basis of standard deviation analysis of the image kernel during filtering. We removed pixels from the kernel with $>1.5\sigma$ deviation from the kernel mean, and then re-applied the filter algorithm on the revised kernel.

A weighting scheme was then applied to the masked, filtered image swaths to emphasize data acquired under optimal viewing conditions (near-nadir to the sensor) and to reduce the effect of scene and mask edges in the mosaic. Weight of an image pixel is computed as the product of a fractional "scan weight" (between 0 and 1), a fractional "mask weight" (between 0 and 1), and a scale factor (50,000). 'Scan weight' is determined by the proximity to the nadir track for the scene: it is set to 1 for the nadir track and zero for the maximum

scan angle. The scan weight image ($W_{\text{final}(i,j)}$) is computed as follows:

$$\phi_{\text{scan}(i,j)} = \arcsin[(R_e/R_{\text{sat}}) * \sin(\phi_{\text{sensor}(i,j)})]; \qquad (1)$$

$$\phi_{\text{scan}_{\text{max}}} = \arcsin[(R_e/R_{\text{sat}}) * \sin(\phi_{\text{sensor}_{\text{max}}})]; \qquad (2)$$

$$W_{\text{scan}(i,j)} = [\cos(\phi_{\text{scan}(i,j)})^2 - \cos(\phi_{\text{scan}_{\text{max}}})^2] \\ /[1 - \cos(\phi_{\text{scan}_{\text{max}}})^2]; \qquad (3)$$

$$W_{\text{mask}(i,j)} = (\Sigma M_{\text{img}(h,k)}/n^2; \qquad (4)$$

$$W_{\text{final}(i,j)} = [W_{\text{scan}(i,j)} * W_{\text{mask}(i,j)}] * K \qquad (5)$$

where $\phi_{\text{scan}(i,j)}$ is the scan angle for the pixel; $\phi_{\text{sensor}(i,j)}$ is the sensor zenith angle for the grid cell (subscript i,j indicates the value is determined for all grid cells); R_e is the radius of the earth (circular approximation of 6371 km), R_{sat} is the radius to the Aqua and Terra platforms ($R_e + 725$ km); $\phi_{\text{sensor\_max}}$ and $\phi_{\text{scan\_max}}$ are the sensor and scan angle values for the maximum scan angle from the spacecraft ($\sim 66°$ and 58.4°, respectively); W_{scan} is the weight factor we assign for a given scan angle; W_{mask} is the weight factor derived from the mask image ($M_{\text{img}(h,k)}$) associated with a given scene (an image of DN = 1 for clear areas, DN = 0 for cloud, ocean, or noise areas). Here h,k indicate the pixel indices for a low-pass filter kernel ($n \times n$, where $n = 43$ pixels) applied to the mask image to reduce the edge effects of the masks in the composite, i.e., 'feathering' the mask edges. The final weight values are scaled to a large $K = 50,000$ two-byte integer to simplify computer image arithmetic. This scaling was removed in post-processing by dividing the two-byte weights by the K scaling factor.

The weight images and the masked high-pass-filtered band 1 images (260 of them) were then combined on a single grid of 125 m spacing covering the entire continent, by, effectively, summing the weighted image grid cell values, and then dividing by the grid cell sum of the mask images. This process of stacking and averaging images on a sub-pixel-sized grid leads to improved spatial and radiometric characteristics in the derived image when the geolocation of the image is significantly better than the scale of the individual scene pixels. This process is called 'image super-resolution' or 'data cumulation' (see Fahnestock et al., 2000a; Scambos et al., 1999; also Hulbe and Fahnestock, 2004 for a discussion of an early version of the MODIS stacking routine). The radiometric improvement is due to combining multiple digital measurements of the surface. The additional spatial resolution in the stacked image composite is a result of knowing the pixel center locations to a high precision (~ 50 m), i.e. a precision that is smaller than the size of the pixel sample area (~ 250 m), and combining the scenes, averaging, and re-gridding, all on a sub-pixel scale grid (125 m for our case).

Images, or intermediate image composites, were added to create the final mosaic by the following scheme. Given two existing band 1 composites, B_0 and B_1, each having C_0 and C_1

count images and associated weight images W_0 and W_1, combined on them already, we create a new composite consisting of C_N, W_N, and B_N:

$$\mathbf{C}_{N(i,j)} = \mathbf{C}_{0(i,j)} + \mathbf{C}_{1(i,j)}; \qquad (6)$$

$$\begin{aligned} \mathbf{W}_{N0(i,j)} &= [\mathbf{W}_{0(i,j)} * \mathbf{C}_{0(i,j)}]/\mathbf{C}_{N(i,j)}; \mathbf{W}_{N1(i,j)} \\ &= [\mathbf{W}_{1(i,j)} * \mathbf{C}_{1(i,j)}]/\mathbf{C}_{N(i,j)}; \mathbf{W}_{N(i,j)} \\ &= \mathbf{W}_{N0(i,j)} + \mathbf{W}_{N1(i,j)} \end{aligned} \qquad (7)$$

$$\mathbf{B}_{N(i,j)} = [\mathbf{W}_{N0(i,j)} * \mathbf{B}_{0(i,j)} + \mathbf{W}_{N1(i,j)} * \mathbf{B}_{1(i,j)}]/\mathbf{W}_{N(i,j)}. \qquad (8)$$

Single scene "composites" have counts of 1 and weights of 1 for all i and j. An initial "null" composite has counts of 0, weights of 0, and band 1 values of 0 for all i and j. Missing data have counts of 0, weights of 0 and band 1 values of 0.

Higher mean weight and higher scene count value generally indicates better spatial resolution and reduced visibility of single-scene artifacts in the final high-passed image composite.

For the final MOA products, the image count ranges from 1 to 38 (Fig. 4a); 98.5% of the imaged area has 6 or more images contributing. Mean image count is 14.7. Areas of lowest image count are the northeastern and far northwestern Ronne Ice Shelf (due to the persistent cloud cover), the ice sheet region between the Executive Committee Range and Crary Mountains in West Antarctica, and the area between the Dome Fuji and Plateau Station camps in the East Antarctic Plateau. For the latter region, local noon occurred during the UT time range for image selection, and the sensor overpasses do not occur near local noon. In addition, the outlying Antarctic islands (Balleny, Peter I, South Orkeny, etc.) and iceberg and fast ice areas included in the mosaic have low image counts, typically 1 to 5.

Using the data cumulation model developed in Scambos et al. (1999) (e.g., their Fig. 4) we infer that final mosaic regions with 5 or more contributing images have resolutions of ~ 200 m or better, up to a best resolution value of ~ 150 m (for 10 or more scenes in high-weight-value areas). Mean weight of the image pixels for the MOA grid cells is 0.6064, ranging from 0.096 to 0.9996 (Fig. 4b with weights scaled by 50,000). A large region of lower weights (0.1–0.2) surrounds the South Pole, because all images are (must be) significantly off-nadir in this area.

Fig. 5 provides a comparison between an individual component image and the final mosaic, and also illustrates the masking and edge 'feathering' weight scheme for the component images. As noted above, the broader range of lighting in the composite image provides a better representation of subtle linear features, and image stacking provides greater radiometric resolution. Additionally, residual banding from the de-striping algorithm is reduced.

2.5. Optical surface grain size composite

A composite image of optical surface grain radius was generated by applying a model-derived look-up table to images of normalized difference MODIS band 1 (red light; 620–670 nm)
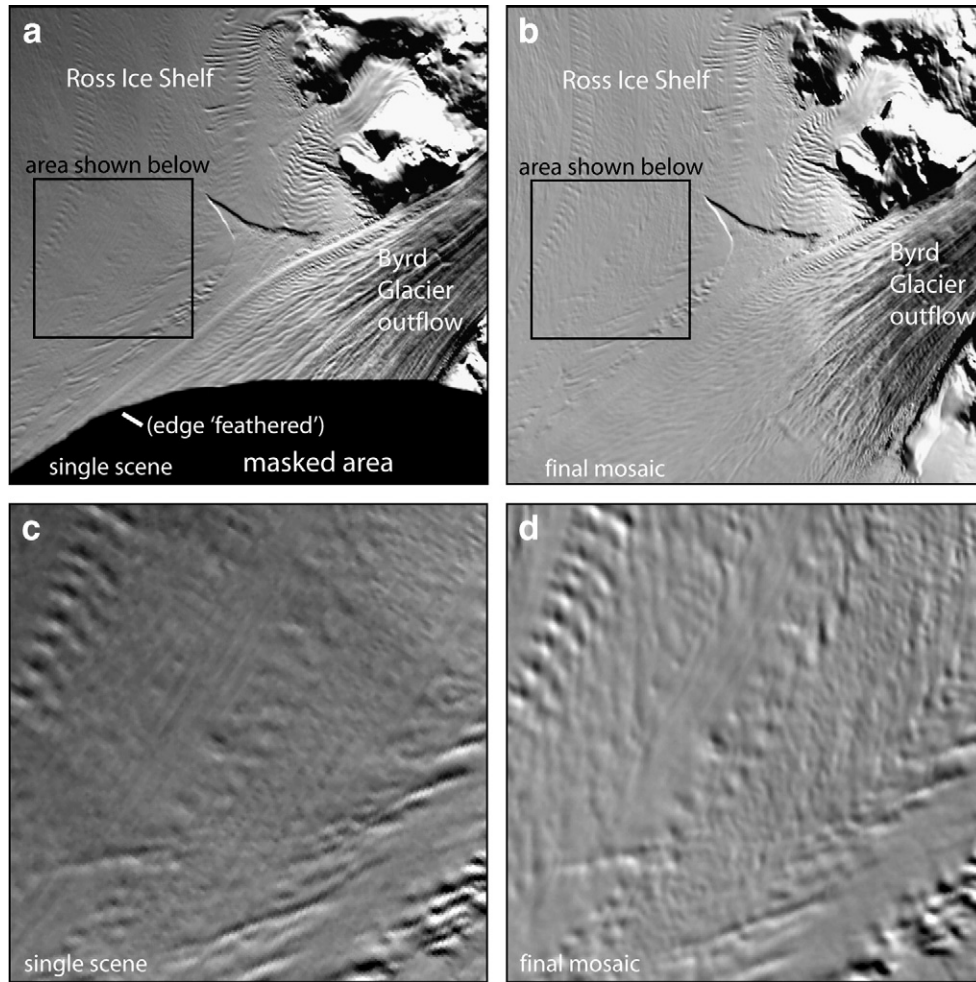
Fig. 5. Comparison of a single processed MODIS scene with the 125 m MOA surface morphology composite image in the region of Byrd Glacier outflow on the Ross Ice Shelf. a) The single MODIS sub-scene (Aqua MODIS sensor, December 6, 2003, 08:00 UT acquisition) has been processed to remove striping, and has the cloud mask applied in the lower portion of the image. The weighting scheme is also evident in both the 'feathering' of the mask edge (brightness ramp applied over 43 pixels) and in a subtle gradient of brightness across the image from left to right. b) The composite image, composed of the Aqua MODIS scene and approximately 30 others, provides a more uniform representation of the surface, and greater detail in the Ross Ice Shelf surface morphology. Upper images are 96 km on a side; lower images are 32 km square.

and MODIS band 2 (near-infrared; 841–876 nm) radiances and solar zenith angle:

$$\mathbf{G}_{i,j} = (b1_{i,j} - b2_{i,j})/(b1_{i,j} + b2_{i,j}) \tag{9}$$

$$\mathbf{S}_{i,j} = f(\mathbf{G}_{i,j}, \mathbf{Z}_{i,j}) \tag{10}$$

where $\mathbf{G}_{i,j}$ is a normalized radiance ratio image, $b1_{i,j}$ and $b2_{i,j}$ are the calibrated band radiance values at grid location (i,j) for the respective MODIS bands, $\mathbf{Z}_{i,j}$ is the solar zenith angle image for each MODIS pixel in the scene, $f(\mathbf{G}_{i,j}, \mathbf{Z}_{i,j})$ is the look-up table, and $\mathbf{S}_{i,j}$ is the optical grain radius image. The normalized difference method subdues the effects of shadows and sub-pixel shadowing due to surface roughness.

The final grain size image is composited from the 260 derived snow-grain images in a similar manner as the surface morphology composite. Calibration scale factors are provided in the MOD02QKM and MYDO2QKM data for the Terra and Aqua MODIS sensors, respectively. These scale factors convert the raw DN values to radiance spectral density in units of W m^{-2} μm^{-1} sr^{-1}. We convert this to radiance (units of W m^{-2} sr^{-1}) by multiplying each band in each sensor by the effective bandwidth in micrometers (μm). These effective bandwidths were determined by integrating the spectral response functions (available at ftp://ftp.mcst.ssai.biz/pub/permanent/MCST) for the bands. We derived Terra bandwidths of 0.04031 and 0.03781 μm for band 1 and band 2, and Aqua bandwidths of 0.04248 and 0.03779 μm.

Look-up table values for the grain size conversion relative to the range of solar zenith angles and atmospheric absorptions in the image observatoins were derived from runs of the Santa Barbara DISORT Atmospheric Radiative Transfer (SBDART) software (Ricchiazzi et al., 1998; see http://www.crseo.ucsb.edu/esrg/sbdart). The calculated radiance ratio for a top-of-the-atmosphere (TOA) observation is sensitive to both water vapor and ozone content of the reference atmosphere. We used the 'sub-arctic winter' reference atmosphere provided in SBDART, but with modified water vapor and temperature profiles to match a January, 2004 atmospheric profile above the Dome

Concordia base in East Antarctica (Hudson et al., 2006, and pers. comm.). Altitude (a scaling factor for absorption effects) was set to 1500 m, a mean value for the continent. Test runs showed that the generated lookup values were relatively insensitive to elevation, i.e., changes in the thickness of the lower atmosphere. We set total ozone content to 270 Dobson Units, a value typical of the 2003–2004 December–January–February levels (e.g., http://cmdl.noaa.gov/ozsonde/spo).

Runs of the SBDART software provided predicted MODIS TOA band 1 and band 2 radiance values for a series of snow grain sizes (10 μm to 1100 μm at 10 μm increments) at a series of solar illuminations in 0.1° increments of solar zenith angle, 0° to 89°. We provided snow optical properties for SBDART runs (i.e. hemispherical–directional reflectance factor, or HDRF, information for the two spectral bands; see Schaepman et al., 2006) from a recent snow reflectance model and created files (one for every 10 μm of grain size) that used this information as the reflecting substrate in the atmospheric radiative transfer model (Painter & Dozier, 2004). This information included Mie single scattering parameters (Mie, 1908) using the *miev0.f* subroutine distributed by W. Wiscome at Goddard Space Flight Center (available at http://atol.ucsd.edu/scatlib/scatterlib.htm), the single scattering albedo, the extinction efficiency, and the Legendre moments for expansion of the single scattering phase function. Snow impurity effects are not considered, and are expected to be very small for Antarctic snow. Sensor viewing angle was held at nadir for all SBDART evaluations, and thus our weighting scheme favoring nadir-viewing conditions, described above, was appropriate to reduce off-nadir HDRF effects in the final optical snow grain size composite, although it does not eliminate them (see validation results below). This approach was chosen as a compromise between addressing the most severe aspects of HDRF effects, while keeping data handling and processing reasonable.

The SBDART-predicted band 1 and band 2 TOA reflectance, for each grain size and each sensor zenith, were then converted to predicted TOA normalized band ratios (G), as discussed above. The predicted G and associated grain sizes were then interpolated into a series of 891 look-up tables (one for each 0.1° bin for solar zenith angle). The tables had 5100 pairs of G and grain-size values, resolved to 0.0001 for G and 1 μm for grain size. Predicted G values range from −0.100 to 0.4099. Values of G that led to un-modeled grain sizes, i.e.<10 μm or >1100 μm, had the associated grain size value set to 'marker' values of 5 μm and 1105 μm, respectively.

These look-up tables were applied to the 260 MOA scenes to produce a corresponding set of grain size images. The grain size images were then composited together using the same weighting and compositing scheme as for the surface morphology image, with the exception that (in addition to masked areas) values of 5 or 1105 μm were treated as missing data. Count images for the grain size composite (not shown) are slightly different from the surface morphology count images because of these additional missing values. In cases where all images gave out-of-range grain size results, the grid cell value was set to 5 μm or 1105 μm. The results of the look-up-table runs of SBDART for the two sensors, Aqua and Terra MODIS, for solar zenith angle >40° are shown in Fig. 6. Superimposed on the Fig. 6 plots is the range of grain sizes of the Antarctic surface snow, firn, and blue ice as mapped by the look-up-table from the MOA images. Additionally, the grain size images from the 260 MOA contributing scenes were used to calculate the standard deviation of the grain size for each pixel, again eliminating the out-of-range grain sizes in the calculation. We did not mask dark shadow, rock, or water areas in the grain size mosaic. The snow grain size index value in these areas is not applicable.

The grain size trends for the two sensors shown in Fig. 6 show that at high solar zenith angle, some grain size measurements, particularly for Terra images, were affected by both off-nadir viewing and the lack of a relative azimuth correction, leading to low or even negative optical grain size values. The observing and illumination conditions that support the generation of an excellent, continent-wide mosaic image of surface morphology (low sun angle, wide scan angle range for
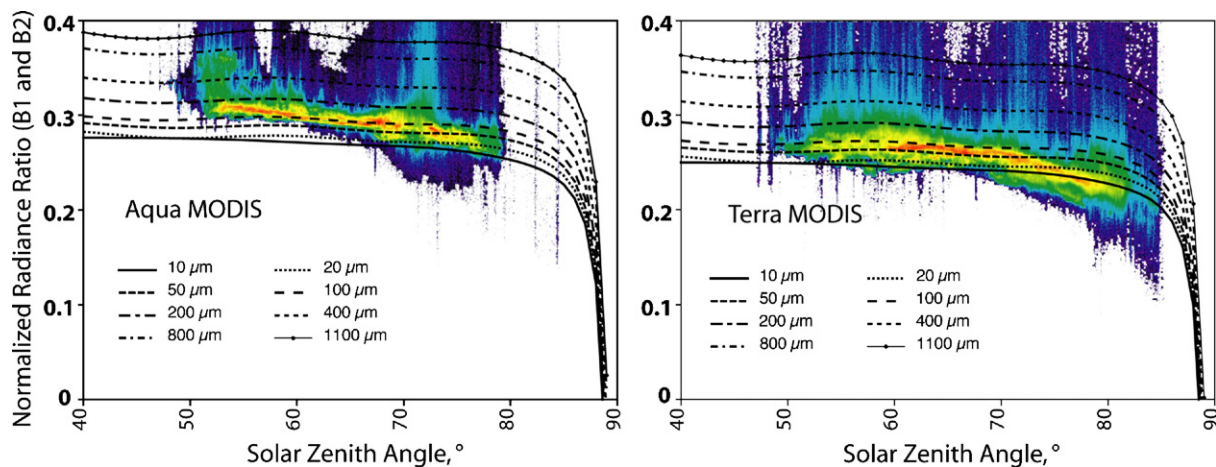

Fig. 6. Grain-size look-up tables, as graphs, for Aqua and Terra normalized radiance ratio values versus solar zenith angle. Superimposed are color data density plots of the same parameters for the composite image pixels for the two sensors (i.e. showing the observed normalized radiance ratios and solar zenith angles for all cloud-cleared areas of the MOA images of the Antarctic surface) and lines of the modeled grain sizes from SBDART data runs. Data density color scale is linear, with warmer colors indicating higher density of measured values.

coverage) are not ideal for snow grain size mapping and HDRF correction. Again, in the compositing, we weighted nadir-viewed areas more strongly, and eliminated non-physical values for snow grain size. If measurements under more favorable viewing conditions were available for the same grid scale, then the computed grain sizes for those observations were used: otherwise the grain size was set to the appropriate out-of-range value (5 or 1105 μm).

The normalized difference band radiance ratio correlates with surface grain size because of the decreasing snow reflectivity in the infrared as grain size increases (see e.g., Fily et al., 1997; Painter & Dozier, 2004; Warren, 1982). In detail, this reflectivity change is due to absorptive interactions between infrared light and ice crystal electronic structure. Decreasing reflectivity in the infrared, the principal observable leading to a remote determination of grain size, is a function of the greater mean absorbing path length within a larger grain, i.e. increased absorption with longer path length through the crystal structure. However, optical path within ice is also a function of grain shape: complex, feathery grains will have a small *optical* grain size even though individual grains may have a much larger maximum dimension. For most albedo or energy balance investigations, optical grain size is the desired parameter because the fundamental physics of the study concerns ice interacting with light (Painter et al., 2007).

Validation data for the optical grain size measurement are shown in Table 1. During three locally clear-sky days in October, 2003, 6 surface snow spectral measurements were made using a field spectrometer as part of the Antarctic Remote Ice Sensing Experiment (ARISE: Massom et al., 2006). Data were collected by averaging 60 spectra of snow (spectral range 0.4 to 2.5 μm), normalized to 40 spectra of an Etalon calibration target. Etalon calibrations and snow surface spectra were acquired in an alternating pattern, minimizing any time-dependent illumination differences. Spectral data were inverted to optically equivalent

grain size radius using conversions developed by Nolin and Dozier (2000) with 50–100 μm grain radius uncertainties. The same sites were imaged by 6 MODIS scenes, 5 from the Terra platform and 1 from Aqua. In situ grain size radius ranged from 66 μm for snow immediately following a storm accumulation to 170 μm for wet snow in warmer conditions. Comparison of predicted grain sizes from the method used above for these images and the in situ spectra shows in general an underestimate of grain size from the satellite algorithm (range 15 to 151 μm). The scale of these differences correlated with high sensor zenith angle; with the satellite in the nadir viewing position (as it was modeled with the SBDART-generated tables), the agreement was relatively good. However, the agreement improved significantly with inclusion of a correction for both sensor zenith angle and relative azimuth, with the majority of the improvement related to sensor zenith angle correction (Table 1, rightmost column). This supports our weighting scheme, favoring nadir-viewing satellite data, but also indicates that future satellite band-ratio optical grain-size mappings should include corrections for sensor viewing angle.

3. Application of the MOA image data products

3.1. Coastline and grounding line data sets extracted from MOA surface morphology image

The MOA surface morphology data product provides both excellent geo-location accuracy and high sensitivity to topographic and albedo features. Although it should be noted that the data values in the data set are not a physical measurement, the images were processed consistently across the entire continent, and data ranges for various surface types are consistent. Known areas of rock or soil (sunlit) have data values ranging between 1900 and 5000 (Dry Valleys, Seymour Island, Vestfold Hills). Blue ice and windswept firn regions

Table 1
Validation measurements of normalized difference radiance ratio and optical snow grain size

Date/site (all in 2003)	In situ solar zenith [a], °	In situ optical SGS, μm	Satellite scene [b]	Satellite solar zenith [c], °	Satellite sensor zenith [c], °	Sat.-Sun relative azimuth [c], °	Satellite NDRR [c]	MOA optical SGS [c], μm	Corrected optical SGS [c], μm
04:48 3 Oct 'snow site a'	61.4	106±50	Terra, 00:50 Terra, 02:30	69.2 62.6	30.7 50.6	66.5 109.2	0.264(2) 0.256(2)	87.4±14 36.0±5	85 130
05:26 3 Oct 'snow site 'b'	61.8	92±50	Terra, 00:50 Terra, 02:30	69.2 62.6	30.7 50.6	66.5 109.2	0.264(2) 0.256(2)	87.4±14 36.0±5	85 130
04:00 7 Oct 'snow site a' (recent precip.)	60.3	66±50	Terra, 00:25 Terra, 02:05	70.8 63.0	51.3 25.1	65.9 110.9	0.243(2) 0.258(3)	15±5[d] 34±12	18.5 55
04:10 7 Oct 'snow site b' (recent precip.)	60.3	75±50	Terra, 00:25 Terra, 02:05	70.8 63.0	51.3 25.1	65.9 110.9	0.243(2) 0.258(3)	15±5[d] 34±12	18.5 55
03:10 20 Oct 'snow site a' (wet snow)	56.3	170±50	Terra, 01:35 Aqua, 07:10	62.2 61.7	18.4 14.9	66.1 112.3	0.282(4) 0.307(3)	151±30 144±25	160 172
03:20 20 Oct 'snow site b' (wet snow)	56.3	271±50	Terra, 01:35 Aqua, 07:10	62.2 61.7	18.4 14.9	66.1 112.3	0.282(4) 0.307(3)	151±30 144±25	160 172

Site locations: October 3, 64° 36.55′ S, 117° 40.17′ E; October 7, 64° 33.32′ S, 116° 34.90′ E; October 20, 65° 16.26′ S, 109° 27.78′ E; same-day sites within 100 m of each other. SGS refers to 'snow grain size'.

[a] All in situ snow spectra-to-grain-size conversions run with 60° solar zenith angle.

[b] UTC time of start of acquisition of 5-minute scene.

[c] Mean of five near-site pixel values; NDRR refers to 'normalized difference radiance ratio'.
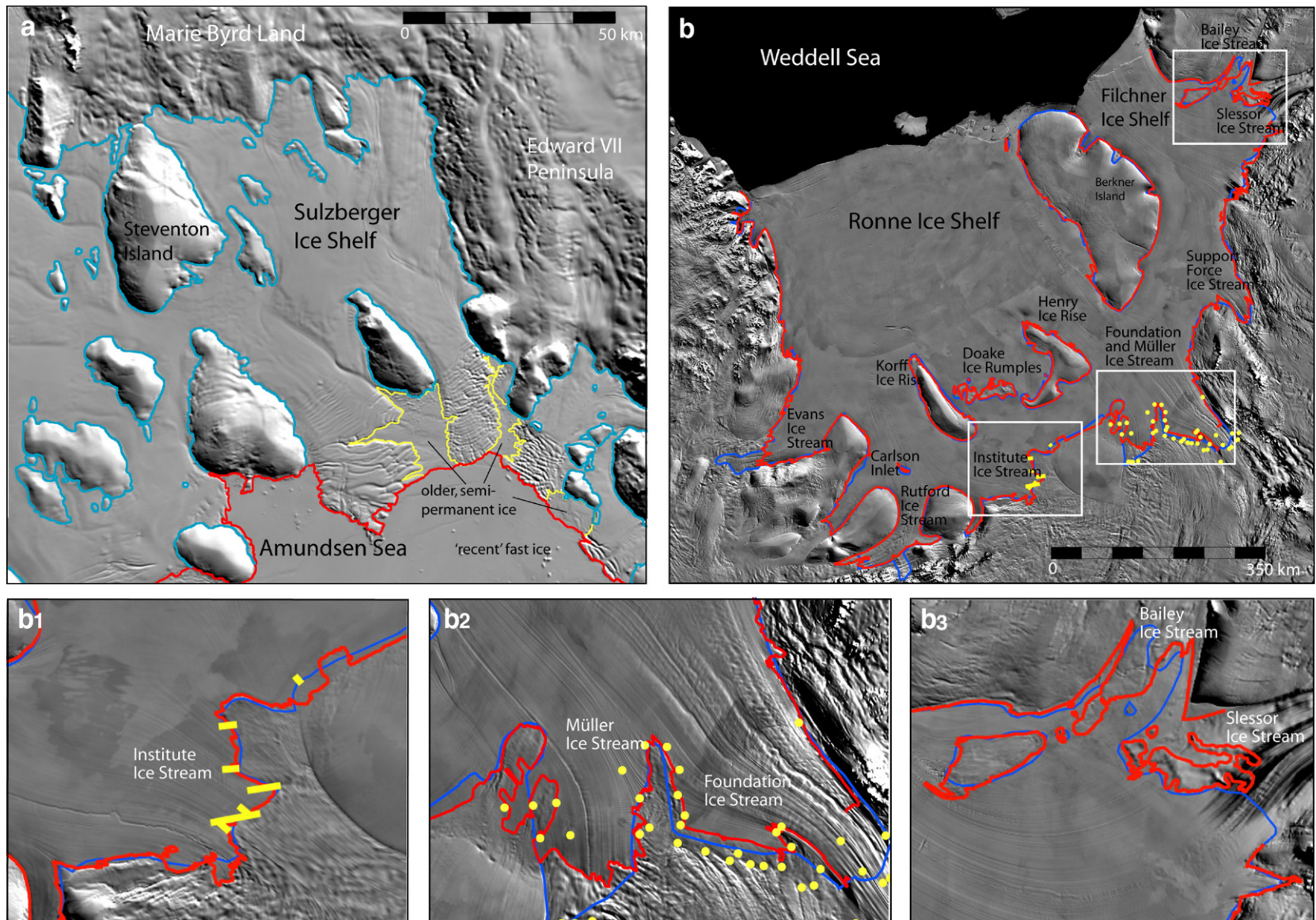
[d] Most pixels showed <10 μm.

Fig. 7. Illustration of the coastline ('permanent' ice) and grounding line (coastal slope break) data sets derived from MOA surface morphology image, for selected areas of the Ronne–Filchner and Sulzberger ice shelves. a) Coastline (red) and grounding line (cyan) data set excerpts for Sulzberger Ice Shelf. Yellow line indicates regions of intermediate-age, multi-decadal ice (not in either data set), included as 'permanent' ice, consistent with past mappings of the coast. b) and b1–b3) Coastal slope break line derived from MOA (red) compared with grounding line from InSAR (blue, Joughin, pers. comm., and Joughin et al., 2006) and ICESat-derived coastal zone mapping (yellow, Fricker, pers. comm., and Fricker & Padman, 2006). Yellow dots mark upstream limit of tidal flexure; yellow lines mark extent of grounding zone. (For interpretation of the references to colour in this figure legend, the reader is referred to the web version of this article.)

range from 8000 to 15,000, and ice sheet snow surfaces range from 14,000 to 17,000 over most areas. Values above 18,000 are typical of sunlight snow slopes in mountain ranges.

The excellent geolocation and slope sensitivity qualities of the MOA surface morphology image make it a useful data set for continent-wide mapping of the coastline (outline of 'permanent' ice and coast) and the grounding line (coastal slope break between floating and grounded ice). Fig. 7 shows some example regions of the grounding line and coastline data sets super-imposed on the MOA surface morphology sub-scene images.

The coastline vector file was manually digitized from the 125 m image grid based on visual interpretation of the boundary between rock, coastal ice wall, or thick 'permanent' floating ice (estimated to be >40 years old, >50 m thick) *versus* ocean, sea ice or short-term fast ice. The coastal slope break line, or grounding line, was similarly digitized by following the seaward-most continuous slope break on the ice surface inside of (or equal to) the permanent ice coastline in highly contrast-enhanced images derived from the MOA surface morphology data set. Location precision of the coastline and grounding line is estimated to be no worse than ±250 m, or two MOA grid cells in the 125 m grid version (i.e., we were able to digitize our estimate of the boundary to this precision).

To confirm our estimates of coastline and costal slope break line, we compared the vector files to existing coastline and grounding line maps of the continent, such as the Antarctic Digital Database file available from British Antarctic Survey (http://www.add.scar.org) and the CIA World Vector Coastline, and to past images such as the USGS AVHRR image mosaic (Ferrigno et al., 1996), and the RAMP AMM-1 and MAMM-2 (Modified Antarctic Mapping Mission 2) mosaic (Jezek, 1999; Liu & Jezek, 2004; K. Farness, 2005 pers. comm.). For the coastline map (near-permanent ice and true coast), we used available, declassified Defense Intelligence Satellite Program (DISP) images and mosaics

(Bindschadler & Seider, 1998) and other coastal change maps (e.g., Swithinbank et al., 1998; 2003) to evaluate a ~40 year 'permanence' of fast ice or shelf ice. Where possible, we checked this with examination of an image archive of AVHRR and MODIS images (http://nsidc.org/iceshelves_images). For ice thickness (>50 m) we used elevation data from the RAMP digital elevation model (Jezek et al., 1999) and profile data from the Ice, Cloud, and land Elevation Satellite (ICESat). Our proxy value for ~50 m ice thickness was a freeboard of at least 10 m (allowing for snow cover). Note that for situations such as the Wilkins Ice Shelf, thought to be composed almost entirely of very old fast ice and in situ accumulation (Vaughan et al., 1993), the distinction between long-term fast ice and an ice shelf is completely obscured. Considering further that ice shelves are likely formed initially from long-lived fast ice during climate cooling periods, we believe that our outline of 'permanent' ice, and our guidelines for mapping it, is consistent with past maps.

The coastline data set, with the example illustrated in Fig. 7a, highlights a current problem in Antarctic ice shelf extent mapping. Detailed satellite image mapping, with digital enhance-ment, makes it apparent that many regions mapped as being within ice shelves are in fact long-term landfast sea ice or a melange of blown-in snow, shelf ice fragments, and marine-derived basal ice. In some areas, the distinction between the older 'permanent' ice and the more ephemeral ice around it is quite large, and so little ambiguity exists (e.g., the Ross Ice Shelf versus the annual- to multi-year fast ice of McMurdo Sound). In other areas, such as the southernmost Larsen Ice Shelf, the Brunt Ice Shelf (Hulbe et al., 2005; Jezek & Liu, 2005), or the Sulzberger Ice Shelf (Fig. 7a), the distinction is less clear. In Fig. 7a, examination of 1960s DISP images, 1970s Landsat images, and AVHRR and MODIS images, shows that fast ice seaward of the red 'coastal ice margin' has retreated in warmer summers, but can
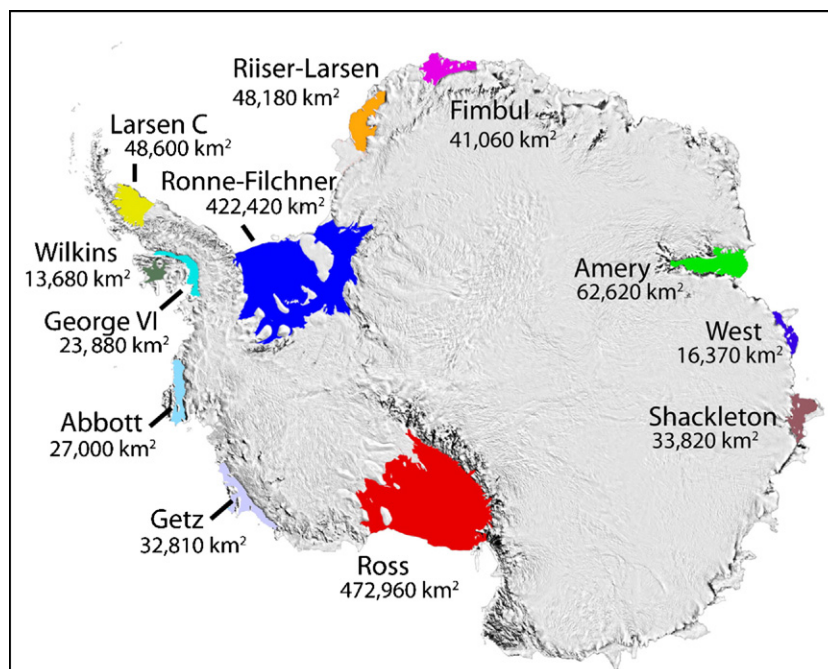

Fig. 8. Ice shelf areas of 11 major ice shelves, 2003–2004, derived from the MOA coastline and grounding line data sets.

persist for several years (Bohlander & Scambos, 2003). Ice on the continent side of the coastal line has never broken up during this period. The yellow outline in Fig. 7a marks what is probably multi-decade fast ice locked within the ice shelf ice. Close inspection shows this ice has been deformed by the shelf ice flowing around it, and thus is becoming integrated into the shelf flow structure. Similar situations occur in the areas mentioned above (southern Larsen Ice Shelf, Brunt Ice Shelf) and several others (West Ice Shelf, Lazarev Ice Shelf), and required decisions regarding the edge of 'permanent' ice.

Fig. 7b and the related sub-scenes provide a comparison of the MOA-derived coastal slope break mapping and grounding line data from ICESat (the Ice Cloud, and land Elevation Satellite) and InSAR (Interferometric Synthetic Aperture Radar) recently determined by Fricker and Padman (2006) and Joughin et al. (2006). These latter two data sets map the grounding line on the basis of the vertical displacement of ice due to tides. The grounding line is actually a region of several kilometers breadth, a 'grounding zone', due to ice flexure and the range of tidal vertical motion (Fricker & Padman, 2006; Vaughan, 1994).

Our 'grounding line' or coastal slope break line file is an approximation of the location of the 'flexure line' in Vaughan's discussion.

3.2. Areas of major ice shelves from the MOA surface morphology data set

We combined the digitized permanent ice coastline and the coastal slope break, or grounding line, to determine the 2003–2004 austral summer ice shelf area for several of the larger ice shelves in Antarctica (Fig. 8). Ice shelf area includes all floating ice within these boundaries (including rifts and melange areas) but excluded all islands, ice rises, and ice rumples. Errors on the total area are estimated from repeat digitizations of the ice extent, and are ±0.15 to 0.25% of the reported area. We note that ice shelf area changes rapidly with shelf flow and calving. For example, area for the Amery is estimated to change by about 270 km^2 per year (a mean speed of 1100 ma^{-1} over 246 km of ice front; see Young & Hyland, 2002), or about 0.4%.
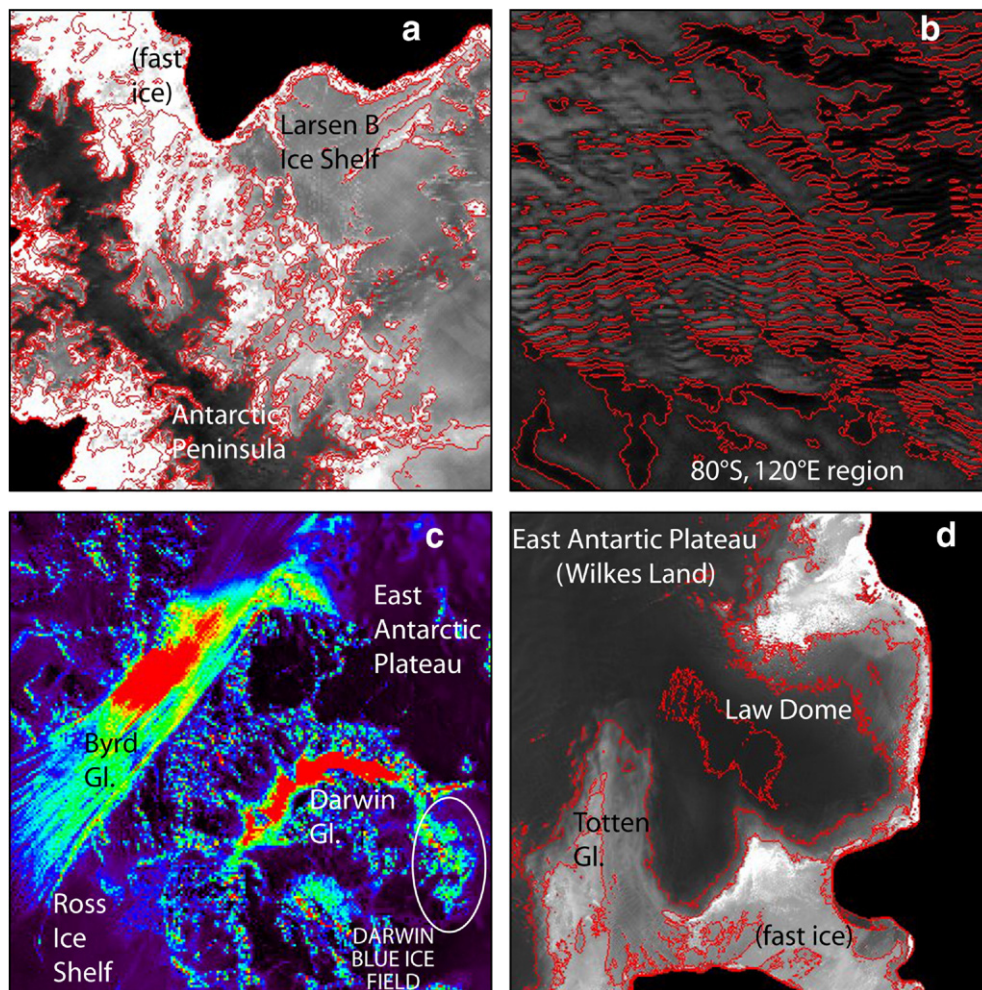

Fig. 9. Grain size maps of selected regions of the Antarctic ice sheet: (a), northern Antarctic Peninsula; (b), megadune region; (c), Byrd Glacier and Darwin Glacier region; (d), Law Dome. Images (a)–(c) each cover 150 by 150 km; image (d) is 300 by 300 km. Contours for (a) and (d) are 100, 200, and 400 μm, scaling with image brightness; contours for (b) are 100 and 150 μm; for (c), red is 1000 μm or greater, cyan is 400 μm, violet is 100 μm, and the finest grain sizes (near black in color) are around 50 μm. (For interpretation of the references to colour in this figure legend, the reader is referred to the web version of this article.)

3.3. Grain size variations and blue ice mapping from the MOA grain size image

The grain size image provides a first-ever look at the variations of mean summer snow grain size over the continent, and reveals several new features (Fig. 1c). The map should be viewed as semi-quantitative estimate of the upper surface (to a few cm depth) mean (multi-date) optical snow grain size, and useful for evaluating the relative climate and precipitation effects on grain size in adjacent areas. Further validation/calibration data, and incorporation of a fuller HDRF correction for our snow grain size algorithm may allow us to improve our grain size estimate for this mapping, or create new mappings. As noted above, the grain size signal from the band-ratio image is modified by surface melt and shadow areas, and in general is a mean of late spring through mid-summer values.

Average optical snow grain radius for the continent from the MOA mapping (all pixels returning a valid mean value between 10 and 1100 μm), is 110±100 μm. Areas of finer snow (15–40 μm) occur north of the West Antarctic Ice Sheet (WAIS) divide, and along the ridge of high elevations between the WAIS summit and the South Pole. East Antarctic Ice Sheet (EAIS) grain sizes above the grounding line elevation tend to be larger, 80–180 μm. EAIS summit and ice divide areas again show lower-end values in this range. Areas of coarser grain size include regions of strong surface melting, surface glaze regions, and blue ice or exposed older firn. We identified regions where melting was likely by comparison to melt-frequency maps based on passive microwave sensitivity (Liu et al., 2006). Standard deviations of grain size increase with mean grain size (but remain relatively constant as a function of normalized difference radiance ratio, the actual measured parameter). Beyond this measurement-related trend, grain size standard deviation is large for areas that see large seasonal variations in grain size, due to frequent melting followed by new snowfall, or in crevasse and blue ice areas. We attribute the higher variability in the latter to the effect of reduced snow bridge or seasonal snow cover (respectively) as the austral summer progresses.

Fig. 9 shows four selected regions of grain size variations as illustrations of both the new data set and the variety of climatological controls of mean grain size. In the Antarctic Peninsula (Fig. 9a), grain size is strongly influenced by elevation and (presumably) temperature, wind ablation, and summer melt severity. Elevated regions of the Graham Land ridge show very fine grain sizes in those regions that remain sub-freezing throughout the summer; grain size values increase in the upper glacier sections presumably due to increased melting (and the influence of warm foehn or chinook winds), and then become still coarser at lower levels due to melt. Crevassed areas also show high optical grain sizes due to exposed blue ice along crevasse walls. The EAIS has broad regions covered by windswept, zero-accumulation 'glaze' areas, and regions of alternating glaze and accumulation called 'megadunes' (Fahnestock et al., 2000b; Frezzotti et al., 2002; Fig. 9b). Megadune regions have distinctive grain size variations, with finer grains (∼90±30 μm) on the windward accumulation faces and coarser grains on the lee faces; the latter

is usually glazed or covered with hoar frost, and have approximately 1.5 times the windward-side grain size (∼135±30 μm). Standard deviations (as a fraction of the grain size value) tend to be lower in the megadunes, and the EAIS in general, due to more stable, persistent summer climate and surface conditions. Fig. 9c, showing grain size variations of Byrd and Darwin Glacier, illustrates a region including very coarse grains due to fractures (in the Byrd Glacier trunk) and wind-driven surface ablation (in Darwin Glacier). Adjacent to Darwin Glacier is a well-known blue-ice meteorite collection field, also named Darwin, showing moderate to coarse grain sizes (400–1100+ μm). Finally, we illustrate a grain-size pattern observed in the MOA optical grain size maps for nearly all coastal ice domes in the EAIS, using Law Dome (Fig. 9d) as an example. Eastward slopes on the upper flanks of the domes have significantly lower grain sizes than equivalent areas on western slopes. This pattern was consistent around the entire EAIS coast, under a variety of viewing and illumination conditions, and by both sensors used in the MOA snow grain size product. We attribute this to more frequent upslope precipitation events on eastern dome flanks in the polar easterly wind pattern.

As a further application of the MOA optical grain size image, in combination with the surface morphology image, we investigated the usefulness of the data set for mapping blue ice regions in Antarctica. Blue ice areas occur for several reasons, such as extensive crevasse exposure, high rates of summer ablation and melting, and high evaporative ablation due to katabatic winds, primarily in the EAIS (Winther et al., 2001). Blue ice regions are known sites of meteorite accumulation, and are thought to be sensitive to climate changes (Bintanja & van den Broeke, 1995). We use a combination of the two main MOA products to select for snow optical grain size and eliminate pixels that have brightness values too low to be blue ice (e.g. shadow or exposed rock). Using the Darwin blue ice region (Fig. 9c, lower right) as a test area, we selected values for brightness that eliminated nearby nunataks, and then used a cutoff for minimum optical snow grain size that gave an area similar to previous measurements of area for the region. A range of 8000 to 15,000 for brightness in the MOA surface morphology product (primarily to eliminate nearby nunataks), and selecting all grid cells with optical grain size >400 μm in the MOA optical snow grain size product, gave a total blue ice area for this region of 219.9 km², very similar to the typical summer value reported for the site using a combination of Landsat and MODIS data (224.3 km², Brown & Scambos, 2004; average of 14 summers in their Table 2). Using these selection criteria, we determined the mean 2003–2004 summertime area of several other meteorite accumulation blue ice regions: Belgica Mountains, 6,442.7 km²; La Paz, 510.8 km²; Grove Mountains, 745.3 km². Moreover, we identified a few high-altitude areas not previously reported as blue ice regions, and not associated with fast ice flow, that met the optical criteria of the other sites: 68.652°S, 132.566°E (9 km²) and 68.233°S, 136.64°E (∼1 km²); 69.606°S, 43.566°E (75.4 km²). Two additional sites in the deep interior of the EAIS also showed anomalously coarse firn, although below the blue ice threshold: 80.676° S,

20.561° E (∼10 km² > 180 μm); 83.606°S, 64.141° E (∼20 km² > 200 μm). Such sites may be new meteorite accumulation regions.

4. Distribution of the mosaic

The two main MOA data products, the surface morphology image and the optical snow grain size image, are available at full 125 m resolution and at 750 m resolution via digital or media transfer from the National Snow and Ice Data Center (NSIDC; Haran et al., 2005). Additionally, several data quality products are available at 750 m resolution, including the mean weight value image, the image count image, mean solar zenith angle images for the Terra and Aqua scenes, and the snow grain size standard deviation image. The coastline and grounding line vector files are available as well. We plan to update these files periodically, and will identify new versions as they are created.

We have developed a map-server website (http://nsidc.org/MMS/moa/moamap.html) that provides the data interactively as user-selected sub-scenes, with several different contrast stretches to highlight different surface or grain size features, and additionally provides other data sets (e.g. the RAMP AMM-1 mosaic image) for comparison. For all these products, we request that users discovering coastline errors, clouds, or other data-quality issues in the provided products please inform NSIDC so that future versions may be improved. NSIDC will also provide the individual component images in the projection, and the cloud and artifact masks, upon request.

5. Summary and future plans

The MOA data products represent a significant improvement in continental satellite mapping of ice sheet surfaces, and introduce several new compiling, assembling, and filtering methods for regional snow and ice surface mapping using MODIS data. The approach taken, incorporating de-striping and de-stitching, uniform range of illumination direction and solar elevation continent-wide, scene-adjusted high-pass filtering to accentuate ice surface features and reduce filter 'ringing' around dark rock areas, stacking of multiple images in a data cumulation scheme, and preservation of grain size information in a separate product, led to better image spatial resolution (∼150 m) and a reduction of noise and surface blemishes relative to true surface morphology. The images show high potential for contributing to research on ice dynamics, climate and precipitation trends, blue ice area mapping, and ice sheet history.

An effort to create a similar map of Greenland and the northeastern Canadian archipelago is underway, using 94 MODIS images from March and April of 2005. This mosaic grid will be designed to match previous and upcoming SAR mosaics of the island, at 100 m spacing. Resolution, however, will still likely be no smaller than ∼150 m in the best areas.

The image data sets are contributing to the improvement of ice sheet digital elevation models (DEMs), using photoclinometry (e.g., Scambos & Haran, 2002). The MOA MODIS image collection already comprises geo-registered, co-gridded images with a variety of solar illumination directions, and

multiple coverage of all pixels, all requirements for an image data set for image enhancement of DEMs in the cited algorithm (Scambos & Haran, 2002).

Moreover, with the necessary software already developed, repeat mappings of both ice sheets are possible. The objectives of re-mapping would be coastal change detection, and outflow rates of the major ice shelves and large outlet glaciers. Given a resolution of 150 m for the best areas of MOA, and a motion sensitivity of 1–2 pixels, we plan to assemble the new mosaics after 4 or 5 summer seasons, permitting ice flow mapping to < 50 ma^{-1}. Some comparisons of this type are already possible using existing continent-wide mosaics (DISP, AVHRR, AMM-1, and MOA).

References

Bindschadler, R.A., & W. Seider (1998). Declassified intelligence satellite photography (DISP) coverage of Antarctica. NASA Technical Memorandum 1998–206879, 37p.

Bindschadler, R. A., & Vornberger, P. L. (1990). AVHRR imagery reveals Antarctic ice dynamics. *Eos, 71*(23), 741−742.

Bindschadler, R. A., Brownworth, F. S., & Stephenson, S. N. (1988). Landsat Thematic Mapper imagery of the Siple Coast, Antarctica. *Antarctic Journal of the United States, 23*(5), 214−215.

Bintanja, R., & van den Broeke, M. R. (1995). The climate sensitivity of Antarctic blue-ice areas. *Annals of Glaciology, 21*, 157−161.

Bohlander, J. A., & Scambos, T. A. (2003). Ice flow and morphology of Prestrud Inlet and Sulzberger Ice Shelf, West Antarctica. *Polar Geography, 26*(3), 227−234.

Bohlander, J., Scambos, T., Haran, T., & Fahnestock, M. (2004). A new MODIS-based Mosaic of Antarctica: MOA. *Eos, Transactions of the American Geophysical Union AGU, 85*(47), F452.

Bourdelles, B., & Fily, M. (1993). Snow grain-size determination from Landsat imagery over Terre Adélie, Antarctica. *Annals of Glaciology, 17*, 86−92.

Brown, I., & Scambos, T. (2004). Satellite monitoring of blue-ice extent near Byrd Glacier, Antarctica. *Annals of Glaciology, 39*, 223−230.

Crabtree, R. D., & Doake, C. S. M. (1980). Flow lines on Antarctic ice shelves. *Polar Record, 20*(124), 31−37.

Dowdeswell, J. A., & McIntyre, N. F. (1987). The surface topography of large ice masses from Landsat imagery. *Journal of Glaciology, 33*(133), 16−33.

Fahnestock, M. A., Bindschadler, R., Kwok, R., & Jezek, K. (1993). Greenland Ice Sheet surface properties and ice dynamics from ERS-1 SAR imagery. *Science, 262*, 1530−1534.

Fahnestock, M. A., Scambos, T. A., Bindschadler, R. A., & Kvaran, G. (2000). A millennium of variable ice flow recorded by the Ross Ice Shelf, Antarctica. *Journal of Glaciology, 46*(155), 652−664.

Fahnestock, M. A., Scambos, T. A., Shuman, C. A., Arthern, R. J., Winebrenner, D. P., & Kwok, R. (2000). Snow megadune fields on the East Antarctic Plateau: Extreme atmosphere-ice interaction. *Geophysical Research Letters, 27*(22), 3719−3722.

Ferrigno, J. G., et al. (1994). Landsat TM image maps of the Shirase and Siple Coast ice streams, West Antarctica. *Annals of Glaciology, 20*, 407−412.

Ferrigno, J. G., et al. (1996). *Satellite image map of Antarctica.U.S. Geological Survey Misc. Survey Series Map I-2560.*

Fily, M., Bourdelles, B., Dedieu, J. P., & Sergent, C. (1997). Comparison of in situ and Landsat Thematic Mapper derived snow grain characteristics in the Alps. *Remote Sensing of Environment*, *59*, 452−460.

Frezzotti, M., Gandolfi, S., La Marcia, F., & Urbini, S. (2002). Snow dunes and glazed surfaces in Antarctica: New field and remote-sensing data. *Annals of Glaciology*, *34*, 81−88.

Fricker, H. A., & Padman, L. (2006). Ice shelf grounding zone structure from ICESat laser altimetry. *Geophysical Research Letters*, *33*. doi:10.1029/2006GL026907

Greene, N., & Heckbert, P. S. (1986). Creating raster omnimax images from multiple perspective views using the elliptical weighted average filter. *IEEE Computer Graphics and Applications*, *6*(6), 21−27.

Haran, T. M., Fahnestock, M. A., & Scambos, T. A. (2002). De-striping of MODIS optical bands for ice sheet mapping and topography. *Eos Transaction of the American Geophysical Union*, *88*(47), F317.

Haran, T., Bohlander, J., Scambos, T., & Fahnestock compilers, M. (2005). *MODIS Mosaic of Antarctica image map and surface snow grain size image. National Snow and Ice Data Center catalogue number 280, digital media.*

Hudson, S. R., Warren, S. G., Brandt, R. E., Grenfell, T. C., & Six, D. (2006). Spectral bidirectional reflectance of Antarctic snow: Measurements and parameterization. *Journal of Geophysical Research*, *111*. doi:10.1029/2006JD007290

Hulbe, C. L., & Fahnestock, M. A. (2004). West Antarctic ice-stream discharge variability: Mechanism, controls, and pattern of grounding-line retreat. *Journal of Glaciology*, *50*(171), 471−484.

Hulbe, C. L., Johnston, R., Joughin, I., & Scambos, T. (2005). Marine modification of fringing ice shelf flow. *Arctic, Antarctic, and Alpine Research*, *37*(3), 323−330.

Jezek, K. (1999). Glaciological properties of the Antarctic ice sheet, from Radarsat-1 Synthetic Aperture Radar Imagery. *Annals of Glaciology*, *29*, 286−290.

Jezek, K. C., & Liu, H. X. (2005). Structure of south-eastern Peninsula ice shelves and ice tongues from synthetic aperture radar imagery. *Journal of Glaciology*, *51*(174), 373−376.

Jezek, K. C., Liu, H. L., Zhao, Z., & Li, B. (1999). Improving a digital elevation model of Antarctica using radar remote sensing data and GIS techniques. *Polar Geography*, *23*(3), 185−200.

Joughin, I., Bamber, J. L., Scambos, T., Tulaczyk, S., Fahnestock, M., & MacAyeal, D. (2006). Integrating satellite observations with modelling: Basal shear stress of the Filchner–Ronne ice streams, Antarctica. *Philosophical Transactions of the Royal Society A*, *364*(1844), 1795−1814.

Liu, H., & Jezek, K. (2004). A complete high-resolution coastline extracted from orthorectified Radarsat SAR imagery. *Photogrammetric Engineering and Remote Sensing*, *70*(5), 605−616.

Liu, H., Wang, Li, & Jezek, K. (2006). Spatiotemporal variations of snowmelt in Antarctica derived from satellite Scanning Multi-Channel Microwave Radiometer and Special Sensor Microwave Imager Data (1978–2004). *Journal of Geophysical Research*, *111*. doi:10.1029/2005JF000318.2

Massom, R., and 17 others (2006). ARISE (Antarctic Remote Ice Sensing Experiment) in the East 2003: Validation of satellite-derived sea-ice data products. *Annals of Glaciology*, *44*, 288−296.

Merson, R. H. (1989). An AVHRR mosaic image of Antarctica. *International Journal of Remote Sensing*, *10*(4–5), 669−674.

Mie, G. (1908). Beitäge zur Optik trüber Medien, Speziell Kolloaidaler Metallösungen. *Annalen der Physik*, *25*, 377−445.

Nolin, A. W., & Dozier, J. (2000). A hyperspectral method fro remotely sensing the grain size of snow. *Remote Sensing of Environment*, *74*(2), 207−216.

Orheim, O., & Lucchitta, B. (1988). Numerical analysis of Landsat thematic mapper images of Antarctica: Surface temperatures and physical properties. *Annals of Glaciology*, *11*, 109−113.

Orheim, O., & Lucchitta, B. (1990). Investigating climate change by digital analysis of blue ice extent on satellite images of Antarctica. *Annals of Glaciology*, *14*, 211−215.

Painter, T. H., Molotch, N., Cassidy, M., Flanner, M., & Steffen, K. (2007). Contact spectroscopy for the determination of stratigraphy of snow grain size. *Journal of Glaciology*, *53*(180), 121−127.

Painter, T., & Dozier, J. (2004). Measurements of the hemispherical–directional reflectance of snow at fine spectral and angular resolution. *Journal of Geophysical Research*, *109*, D18115. doi:10.1029/2003JD004458

Parrish, T., & Bromwich, D. (1991). Continental-scale simulation of the Antarctic katabatic wind regime. *Journal of Climate*, *4*, 135−146.

Ricchiazzi, P., Yang, S., Gautier, C., & Sowle, D. (1998). SBDART: A research and teaching software tool for plane-parallel radiative transfer in the Earth's atmosphere. *Bulletin of American Meterological Society*, *79*(10), 2101−2114.

Scambos, T. A., & Bindschadler, R. A. (1991). Feature map of Ice Streams C, D, and E, West Antarctica. *Antarctic Journal of the United States*, *26*(5), 312−314.

Scambos, T. A., & Haran, T. (2002). An image-enhanced DEM of the Greenland ice sheet. *Annals of Glaciology*, *34*, 291−298.

Scambos, T., Kvaran, G., & Fahnestock, M. (1999). Improving AVHRR resolution through data cumulation for mapping polar ice sheets. *Remote Sensing of Environment*, *69*, 56−66.

Seko, K., Furukawa, T., Nishio, F., & Watanabe, O. (1993). Undulating topography on the Antarctic ice sheet revealed by NOAA AVHRR images. *Annals of Glaciology*, *17*, 55−62.

Schaepman, G., Schaepman, M., Painter, T. H., Dangel, S., & Martonchik, J. (2006). Reflectance quantities in optical remote sensing — Definitions and case studies. *Remote Sensing of Environment*, *103*(1), 27−42.

Simmonds, D. A. (1986). Flow of the Brunt Ice Shelf, Antarctica derived from Landsat images, 1974–1985. *Journal of Glaciology*, *32*(111), 252−254.

Stephenson, S. N., & Bindschadler, R. A. (1990). Is ice-stream evolution revealed by satellite imagery? *Annals of Glaciology*, *14*, 273−277.

Swithinbank, C., Brunk, K., & Sievers, J. (1988). A glaciological map of Filchner–Ronne Ice Shelf, Antarctica. *Annals of Glaciology*, *11*, 150−155.

Swithinbank, C. (1988). Satellite image atlas of glaciers of the world. *Antarctica. U. S. Geological Survey Proffessional Paper, vol. 1386-B.* (pp. 1−138).

Swithinbank, C., R. Williams, J. Ferrigno, K. Foley, C. Halam, & C. Rosanova, 1998. Coastal change and glaciological map of the Saunders Coast area, Antarctica, 1972−1997. U.S. Geological Survey Map I-2600-G.

Swithinbank, C., R. Williams, J. Ferrigno, K. Foley, & C. Rosanova, 2003. Coastal change and glaciological map of the Bakutis Coast area, Antarctica, 1972_1997. U.S. Geological Survey Map I-2600-F (2nd edition).

USGS (1991). Satellite Image Map of Antarctica, 1:5,000,000. Miscellaneous Map Investigation Series, I-2284.

Vaughan, D. G. (1994). Investigating tidal flexure on an ice shelf using kinematic GPS. *Annals of Glaciology*, *20*, 372−376.

Vaughan, D. G., Mantripp, D. R., Sievers, J., & Doake, C. S. M. (1993). A synthesis of remote sensing data on Wilkins Ice Shelf, Antarctica. *Annals of Glaciology*, *17*, 211−218.

Warren, S. (1982). Optical properties of snow. *Reviews of Geophysics and Space Physics*, *20*(1), 67−89.

Winther, Jan-G., Jespersen, M. N., & Liston, G. E. (2001). Blue-ice areas in Antarctica derived from NOAA AVHRR satellite data. *Journal of Glaciology*, *47*(157), 325−334.

Wolfe, R. E., Nishihama, M., Fleig, A. J., Kuyper, J. A., Roy, D. P., Storey, J. C., & Patt, F. S. (2002). Achieving sub-pixel geolocation accuracy in support of MODIS land science. *Remote Sensing of Environment*, *83*(1–2), 31−49.

Young, N., & Hyland, G. (2002). Velocity and strain rates derived from InSAR analysis over the Amery Ice Shelf, East Antarctica. *Annals of Glaciology*, *34*, 228−234.